Applied Ocean Research 152 (2024) 104198

Contents lists available at ScienceDirect

Applied Ocean Research

journal homepage: www.elsevier.com/locate/apor

Research paper

Analytical gradients of first-order diffraction and radiation forces for design optimization of floating structures

Peter J. Rohrer *, Erin E. Bachynski-Polić

Department of Marine Technology, Norwegian University of Science and Technology, Jonsvannsveien 82, Trondheim, 7050, Norway

ARTICLE INFO

Keywords:
Boundary element method
Gradient-based optimization
Implicit analytic derivatives
Surrogate model

ABSTRACT

Gradient-based design optimization of floating structures with many design variables requires efficient and accurate computation of hydrodynamic coefficients including wave excitation forces and their derivatives with respect to design variables. For large-volume structures or structures with many component members, the only practical method to determine diffraction and radiation forces is to apply a boundary element method solver. This work presents the first known boundary element method solver with implicit analytic derivatives, allowing for total derivative computation alongside force evaluation. Two case studies are presented: a single floating circular column and a structure with multiple square columns attached to a horizontal pontoon. Force results from both case studies agree well with reference data, while derivative results agree with the best comparisons available. Computational requirements limit the applicability of this method and suggest further work is required to refine this approach.

1. Introduction

Future applications of floating structures, such as floating offshore wind, offshore aquaculture, and coastal infrastructure will require the implementation of novel substructure concepts. Efficiently designing these substructures requires understanding the first-order hydrodynamic loads on the structure, especially the diffraction forces from incoming waves and radiation forces from motions of the structure. Design optimization offers an efficient and systematic approach to finding the best possible substructure design. As more design variables are used in an optimization problem, algorithms that consider gradients of the optimization objective and constraints with respect to the design variables provide significant performance improvements. For problems beyond a certain scale, often on the order of ten design variables, gradient-free methods become intractable (Martins and Ning, 2021, Chapter 1).

Previous gradient-based design optimization studies for floating structures have most often considered floating wind turbine design. Various methods have been employed to find hydrodynamic coefficients (wave excitation, frequency-dependent added mass, radiation damping) and their derivatives. Fylling and Berthelsen (2011) developed an early gradient-based design optimization tool that used a proprietary tool to compute hydrodynamic coefficients. Derivatives of responses were computed using a finite difference approach, though the authors noted this was a source of error. Dou et al. (2020) developed a gradient-based optimization model for a spar buoy using the QuLAF model (Pegalajar-Jurado et al., 2018) with Morison-type hydrodynamic excitation and sensitivity analysis based on derivatives of the equation of motion. Pollini et al. (2023) extended this QuLAF-based optimization using Morison-type loads to the TetraSpar, a structure with multiple cylindrical components. Hegseth et al. (2020) developed a gradient-based optimization model capable of considering nearly 100 design variables for a spar-buoy platform that used MacCamy–Fuchs's theory (see Section 2.1.2) to find diffraction forces and a strip theory approximation of added mass. Total derivatives were computed in the OpenMDAO framework using a coupled implicit analytic total derivative method. In previous work by the authors Rohrer et al. (2022, 2023), Hegseth's gradient-based model was extended to structures with horizontal members using Morison-type excitation and considering generic modal response for flexible structures. A recent review by Sykes et al. (2023) found no examples of floating wind turbine design optimization that included a differentiated BEM solver, or any other approach that could provide accurate wave excitation loads and their gradients for generic large-volume or multiple column structures.

Surrogate models, or models used to predict hydrodynamic coefficients based on many simulation results, have also been applied to floating wind turbine analysis and design optimization. Kalimeris (2023) developed surrogate models for optimization of a multiple column floating wind turbine substructure. One of the surrogate models used two inputs: column diameter (constant over the length of the

* Corresponding author.
E-mail addresses: peter.j.rohrer@ntnu.no (P.J. Rohrer), erin.bachynski@ntnu.no (E.E. Bachynski-Polić).

https://doi.org/10.1016/j.apor.2024.104198
Received 8 May 2024; Received in revised form 23 July 2024; Accepted 21 August 2024

column) and distance between columns as inputs, and the hydrodynamic coefficients as outputs. The training data included 350 samples obtained using a Python wrapper of HAMS (Liu, 2019), an open-source boundary element method (BEM) solver. Kalimeris found that this surrogate model captured hydrodynamic coefficients well, albeit with some noise. Ilardi et al. (2024) developed a surrogate model trained on 28125 BEM runs to predict hydrodynamic coefficients of spar-buoys with varying radii along the length of the column. While not applied to design optimization, the hydrodynamic coefficients generally agree with BEM results, though a limited range of frequencies and coefficients were presented. The hydrodynamic coefficients, especially frequency-dependent added mass, show significant noise in the key wave frequency range.

As an alternative to surrogate models trained for a single design, some methods have attempted determine hydrodynamic coefficients by interpolation and combination of components or base platform designs. Hall et al. (2014) assumed hydrodynamic properties of large-volume and multiple column platforms could be approximated by linear combinations of six basis platform designs. This assumption and the resulting optimization studies performed well when interactions between component members were less significant. Alonso Reig et al. (2023) developed a method to estimate hydrodynamic coefficients for multiple column structures by interpolating in a database of component members and superimposing the component-level coefficients. Correction terms for column interaction were applied and achieved reasonable agreement with a full BEM solution, though this method was not implemented in an optimization loop.

Outside of studies on floating wind turbines, design optimization approaches for arrays of wave energy converters by Sharp and DuPont (2016) and approaches for control co-design of wave energy converter by Coe et al. (2020) both incorporated a BEM solver in the optimization loop, and made use of gradient-free optimization techniques. McCabe et al. (2022) developed a tool for gradient-based optimization of wave energy converters, but relied on closed-form linear approximations of hydrodynamic coefficients. Zhang et al. (2020) developed a kriging surrogate model for determining hydrodynamic coefficients of arrays of wave energy converters. They found that a direct surrogate model struggled to overcome issues of dimensionality, but a hierarchical surrogate model predicted diffraction forces very well for the array of structures. This hierarchical surrogate incorporated physical knowledge of the array of structures and predicted the additive effect of each additional structure added to the array. The hierarchical surrogate model was applied to a wave energy converter layout optimization problem by Zhang et al. (2020) with only four design variables and a gradient-free optimization algorithm. The surrogate model performed better than an approximate method and nearly as well as the exact solution, but gradient-based optimization was not attempted.

Analytic gradients of hydrodynamic loads have been developed previously for hydrostructural optimization of hydrofoils in work by Liao et al. (2020, 2021) and Ng et al. (2022). Work by Liao et al. made use of high-fidelity computational fluid dynamics flow solvers, while Ng et al. implemented lower-order hydrofoil models. Neither of these methods are directly applicable to developing analytic gradients of diffraction and radiation forces for large-volume structures.

This work presents a differentiated BEM solver that provides accurate diffraction and radiation forces and derivatives that can be used for design optimization. To the authors' knowledge, this is the first such solver that includes analytical derivative computation. These forces and their analytical derivatives enable the use of gradient-based optimization tools and allow for a greater number of design variables (Martins and Ning, 2021, Chapter 1). Analytical derivative computation is considerably more accurate than finite difference approximations and very efficient, as the cost of derivative computation does not scale directly with the number of design variables (Martins and Ning, 2021, Chapter 6).

A description of the key theoretical background for this differentiated BEM solver (referred to as DBEMS) is given in Section 2. The design of the solver, described in more detail in Section 3, largely follows that of other open-source BEM solvers. Several key modifications are made to allow derivative computation, and exact partial derivatives are defined for every step of the solver. Two case studies are presented in Section 4 demonstrating the capability and limitations of DBEMS. Forcing and derivatives are compared to other existing approaches. Finally a discussion of the limitations of the solver and potential future improvements is presented in Section 5.

2. Theory

2.1. Methods for determining hydrodynamic excitation forces in early design

Responses of most floating offshore structures in waves are dominated by first-order excitation loads (Faltinsen, 1998, Chapter 1). Some engineering models also include approximations of higher-order effects, however, for this work, only first-order wave excitation loads are of interest. Two common approaches for determining wave excitation at an early design stage or for optimization are presented here: the boundary element method and a combination of empirical and analytical solutions for component-level loads.

2.1.1. Boundary element method approach

The boundary element method (BEM), also known as the panel method, is a technique for determining fluid–structure interaction based on linear potential flow theory. This method can be applied to an arbitrarily shaped floating structure. The fluid is assumed to be incompressible and inviscid, and its motion is irrotational. The fluid velocity vector $\vec{v}$ at a given point in space $\boldsymbol{x}(x, y, z)$ and time t can be described with a single scalar potential $\boldsymbol{\Phi}(\boldsymbol{x}, t)$ that satisfies the Laplace equation (Eq. (1)) over the entire fluid domain, Ω as shown in Fig. 1. The total potential $\boldsymbol{\Phi}$ is a sum of the incident wave potential ϕ_0, the diffracted wave potential ϕ_D, and the radiated wave potential ϕ_R.

$$\nabla^2 \boldsymbol{\Phi} = 0 \tag{1}$$

A linearized boundary-value problem is created by introducing several boundary conditions to the governing Laplace equation, as illustrated in Fig. 1. The first is a linearized free-surface boundary condition, Eq. (2) applied on S_{FS}, which is equivalent to the combination of kinematic and dynamic free-surface conditions from linear wave theory. For infinite water depth, Eq. (3) represents the bottom boundary condition applied on S_{SB}. Finally, the body boundary condition, Eq. (4), requires that the velocity of the body surface (S_B) equals the velocity of the fluid at the body surface at the mean body position and water level. In Eq. (4), $\vec{n}$ represents the normal vector on the body surface and $\vec{u}$ represents the normal fluid velocity on the body surface. A far-field boundary condition (on S_∞) is also needed to solve the boundary-value problem, as well as initial conditions if a time-domain solution is to be computed.

$$g\frac{\partial \boldsymbol{\Phi}}{\partial z} - \omega^2 \boldsymbol{\Phi} = 0 \qquad \text{on } z = 0 \tag{2}$$

$$|\nabla \boldsymbol{\Phi}| \to 0 \qquad \text{when } z \to -\infty \tag{3}$$

$$\nabla \boldsymbol{\Phi} \cdot \vec{n} = \vec{u} \cdot \vec{n} \qquad \text{on } S_B \tag{4}$$

Two distinct boundary-value problems can be solved by applying different normal velocities on the body surface in Eq. (4). For the diffraction problem $\vec{u}$ is zero (so $\phi_R = 0$) while the total potential $\boldsymbol{\Phi}$ is the sum of the unknown diffraction potential ϕ_D and the incoming linear wave potential ϕ_0 given in Eq. (5). Here g is gravitational acceleration, a is the incident wave amplitude, ω is the incident wave frequency, β is the incident wave angle, and k is the wave number, determined in deep-water by the dispersion relationship given in Eq. (6).

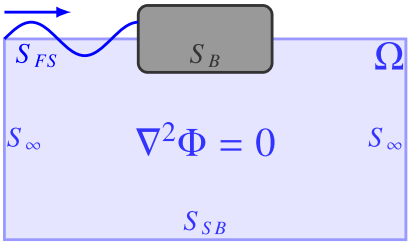

Fig. 1. Diagram of boundary-value problem solved using the BEM.

The radiation problems can be solved for every degree of freedom the body has by setting the velocity in the body boundary condition, Eq. (4), to the velocity of the body in that degree of freedom and solving for the total potential, Φ, with no incident wave. Finally, the Froude–Krylov forces from the incident wave can be found based on incident wave potential in Eq. (5) without solving the boundary value problem.

$$\phi_0 = \frac{iga}{\omega} e^{ikz} e^{-ikx\cos\beta - iky\sin\beta} e^{i\omega t} \tag{5}$$

$$\omega^2 = kg \tag{6}$$

To solve the boundary-value problem, a Green function that satisfies the free surface condition (Eq. (2)) and the sea bottom condition (Eq. (3)) is introduced. Several variations of the Green function are possible. A general form of the Green function for deep water (based on a formulation from Newman (Newman, 2017, Chapter 4)) is given in Eq. (7). The Green function gives the velocity potential at a point $\boldsymbol{x}(x, y, z)$ due to a source at the point $\boldsymbol{\xi}(\xi, \eta, \zeta)$. The first term (Eq. (8)) corresponds to a source term at point $\boldsymbol{\xi}$ while the second term (Eq. (9)) corresponds to a source term at $\boldsymbol{\xi}$ reflected about the free surface, satisfying the infinite water depth bottom boundary condition. The final term, $H(\boldsymbol{x};\boldsymbol{\xi})$, is introduced to satisfy the linearized free-surface boundary condition and the body boundary conditions.

$$G(\boldsymbol{x};\boldsymbol{\xi}) = \frac{1}{r} + \frac{1}{r'} + H(\boldsymbol{x};\boldsymbol{\xi}) \tag{7}$$

$$\frac{1}{r} = \frac{1}{\sqrt{(x-\xi)^2 + (y-\eta)^2 + (z-\zeta)^2}} \tag{8}$$

$$\frac{1}{r'} = \frac{1}{\sqrt{(x-\xi)^2 + (y-\eta)^2 + (z+\zeta)^2}} \tag{9}$$

Using this Green function, the radiation or diffraction potential on the surface of the body can be written as a function of the source distribution, $\sigma(\boldsymbol{x})$, as in Eq. (10) for the diffraction potential. This is known as the indirect method or source formulation. The gradient of the potential on the body surface (with normal vector $\vec{n}$) can also be written as a function of the source distribution, as in Eq. (11). The term $\frac{\sigma(\boldsymbol{x})}{2}$ in Eq. (11) arises due to integration over the singularity introduced at $\boldsymbol{x}$.

$$\phi_D(\boldsymbol{x}) = \iint_\Gamma \sigma(\xi) G(\boldsymbol{x};\xi)\mathrm{d}S(\xi) \tag{10}$$

$$\frac{\partial\phi_D}{\partial\vec{n}}(\boldsymbol{x}) = \frac{\sigma(\boldsymbol{x})}{2} + \iint_\Gamma \sigma(\xi)(\nabla G(\boldsymbol{x};\xi)\cdot\vec{n})\mathrm{d}S(\xi) \tag{11}$$

Several methods have been developed for discretization and computation of the Green functions and their surface integrals. The specific methods used in this work are discussed in Section 3.1.

2.1.2. Empirical and analytical methods

A common approach in engineering tools is to approximate the hydrodynamic excitation using the empirical MOJS (Morison's) equation (Morison et al., 1950) or the analytical solution of the diffraction problem proposed by MacCamy and Fuchs (1954). Both methods were originally developed for determining wave excitation on surface piercing cylindrical piles, but have been shown to be suitable for more generic applications involving bodies in waves. These methods are often combined with a strip theory approach based on constant added mass terms to compute total added mass, while radiation damping is neglected. Alternatively, for simple geometries, analytical expressions for added mass and radiation damping are available, such as those developed by Yeung (1981) for vertical cylinders. The main reason for using an empirical or analytical approach is very fast computation using closed-form equations and a basis in the fundamental physics of the problem.

Morison's equation. Morison's equation is a semi-empirical formulation for wave excitation that combines an inertia force proportional to wave particle acceleration and a drag force proportional to the square of wave particle velocity (Morison et al., 1950). For example, horizontal and vertical forces on a horizontal cylinder with axis orthogonal to the incoming wave (normal forces) can be expressed by Eqs. (12) and (13), respectively, using the form from Faltinsen (1998, Chapter 7). Here $\mathrm{d}F_1$ is the horizontal force contribution and $\mathrm{d}F_3$ is the vertical force contribution for a strip of length $\mathrm{d}y$ and diameter D. The wave particle accelerations are a_1, a_3 and velocities u, w in the horizontal and vertical directions, respectively. This normal force formulation can be further extended for strips with arbitrary orientation, while the tangential force is typically replaced by a Froude–Krylov force on the cylinder's base.

$$\mathrm{d}F_1 = \rho\frac{\pi D^2}{4}\mathrm{d}yC_M a_1 + \frac{\rho}{2}C_D D\mathrm{d}yu\sqrt{u^2+w^2} \tag{12}$$

$$\mathrm{d}F_3 = \rho\frac{\pi D^2}{4}\mathrm{d}yC_M a_3 + \frac{\rho}{2}C_D D\mathrm{d}yw\sqrt{u^2+w^2} \tag{13}$$

In Eqs. (12) and (13), C_M and C_D are the mass coefficient and drag coefficient, respectively. For comparison to other methods (BEM, MacCamy–Fuchs) that do not include a drag term, the drag coefficient can simply be set equal to zero.

MacCamy–Fuchs theory. MacCamy and Fuchs developed an exact solution to the diffraction problem for vertical bottom-fixed circular cylinders based on earlier solutions for electromagnetic and sound waves (MacCamy and Fuchs, 1954). The force expression they developed (Eq. (14)) gives horizontal force per unit length ($\mathrm{d}F_1$) at depth z for a given wave amplitude a, wave number (following Eq. (6)) k, wave frequency ω, water depth H, and cylinder radius r. The phase α given in Eq. (15) and amplitude $A(kr)$ given in Eq. (16) include the derivatives of Bessel's functions of the first kind (J_1') and second kind (Y_1').

$$\mathrm{d}F_1 = \frac{4\rho ga}{k}\frac{\cosh k(H+z)}{\cosh kH}A(kr)\cos(\omega t - \alpha) \tag{14}$$

$$\tan\alpha = \frac{J_1'(\pi kr)}{Y_1'(\pi kr)} \tag{15}$$

$$A(kr) = \frac{1}{\sqrt{J_1'^2(\pi kr) + Y_1'^2(\pi kr)}} \tag{16}$$

Further work by Linton and Evans (1993) extended MacCamy–Fuchs's theory to multiple vertical cylinders arranged in an array, meaning diffraction effects between these cylinders can be considered. For selected geometries, analytical solutions have been developed for both horizontal and vertical forces. Garrett (1971) developed an analytical solution for a floating circular cylinder which is consistent with MacCamy and Fuchs's theory for a cylinder extending to the sea bottom.

Forces on the base of floating vertical cylinders (the surface parallel to the free surface) cannot be easily computed using either Morison's equation or MacCamy–Fuchs theory. A typical approach for these surfaces is to compute the Froude–Krylov force, or the force due to the undisturbed pressure field caused by the incident wave. This is neither an empirical model nor an analytical solution to the diffraction

problem, but rather an extension of linear wave theory. The dynamic pressure due to the incident wave is the fluid density multiplied by the derivative of incident wave potential from Eq. (5) with respect to time. The vertical force per unit area is then simply the dynamic pressure multiplied by the area.

To model wave excitation on realistic floating structures, some combination of these three approaches is typically needed. Fig. 2 illustrates a combined Morison/MacCamy–Fuchs/Froude–Krylov approach for a structure with a vertical surface-piercing column and horizontal pontoons. Morison loads (F_{Mor}) are applied to the pontoons, MacCamy–Fuchs (F_{McF}) to the column, and Frode–Krylov (F_{FK}) to the column base and pontoon ends. For many structures dominated by slender elements, this approach can give reasonable agreement with a full potential flow theory solution — especially at low wave frequencies. These approaches all offer the benefit of having closed-form equations that can be exactly differentiated.

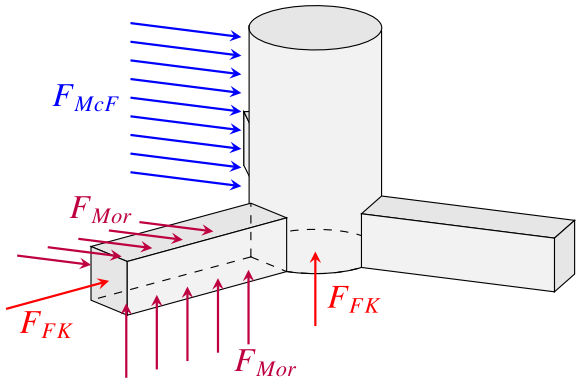

Fig. 2. Diagram of hypothetical combined empirical and analytical forcing model for floating structure.

2.2. Methods for determining derivatives

Several methods are commonly used for determining derivatives in numerical models depending on the amount of information available about the model and its characteristics. Three categories of methods exist: those that require no information about the model, those that require every line of code in the model, and those that require only the model's states and residuals. Generally, differentiation methods that require more information about the model can produce more accurate derivatives more efficiently. Algorithmic differentiation, which requires line-by-line modification to source code, was not considered for this work. The implementation effort required to develop or modify a BEM code to be compatible with algorithmic differentiation was deemed to be greater than that of implicit analytic total derivative computation using exact partial derivatives, with similar accuracy and computational efficiency. The complex step method, a form of algorithmic differentiation using complex numbers to compute derivatives, was also not implemented due to extensive modifications needed to handle the complex operations in a BEM code. A more thorough description of available methods is given by Martins & Ning (Martins and Ning, 2021, Chapter 6) among other sources.

2.2.1. Finite differences

Derivatives based on finite differences have the most straightforward theoretical background — the derivative at a point is equivalent to the change in the function after a small perturbation divided by the step size of that perturbation. This method requires no knowledge of the model, and therefore can be applied on a 'black box' model. This is especially useful for models that require closed-source packages or perform calculations that are difficult to differentiate. Finite difference approaches can be also be developed for higher-order derivatives and directional derivatives (Martins and Ning, 2021, Chapter 6). Although simple and straightforward to implement, the computational demands of the finite difference method grows as the number of design variables increases, and truncation errors and subtractive errors limit their accuracy (Martins and Ning, 2021, Chapter 6).

2.2.2. Implicit analytic methods

Implicit analytic methods for total derivatives make use of the residuals and states of the model to very efficiently compute total derivatives with the same accuracy as function evaluation. These methods find derivatives by solving a system of equations developed by linearizing the model's governing equation. Any numerical model can be rewritten as a system of states and residuals in the form $r(u; x) = 0$, where the residuals are a function of model states u and inputs x — which are fixed when solving for states.

The total derivatives of interest are of the outputs of the function of interest with respect to the inputs, which can be written as Eq. (17) based on the chain rule. Each of the partial derivative terms here are relatively easy and cheap to compute — as they represent change in the function but do not necessarily satisfy the governing equations.

$$\frac{\mathrm{d}f}{\mathrm{d}x} = \frac{\partial f}{\partial x} + \frac{\partial f}{\partial u}\frac{\mathrm{d}u}{\mathrm{d}x} \tag{17}$$

Computing the total derivative of the states with respect to inputs ($\mathrm{d}u/\mathrm{d}x$) requires consideration of the governing equation — specifically that the total differential of the residual must equal zero for the governing equation to be satisfied. Based on this, the total differential for the residual can be rearranged as in Eq. (18), and the total derivative (Eq. (17)) can be rewritten as Eq. (19).

$$\frac{\partial r}{\partial u}\frac{\mathrm{d}u}{\mathrm{d}x} = -\frac{\partial r}{\partial x} \tag{18}$$

$$\frac{\mathrm{d}f}{\mathrm{d}x} = \frac{\partial f}{\partial x} - \frac{\partial f}{\partial u}\frac{\partial r}{\partial u}^{-1}\frac{\partial r}{\partial x} \tag{19}$$

Again, the partial derivative terms in Eq. (18) are relatively cheap to compute. In many cases the partial derivatives can computed exactly. The total derivative is then computed by solving the linear system in the second term on the right hand side of Eq. (19).

2.3. Surrogate modeling approach

Surrogate modeling refers to the development of an approximate model that describes another model. The approximate model is less computationally intensive or has other useful properties such as continuity, a closed-form expression, or straightforward derivative computation (Martins and Ning, 2021, Chapter 10). Several forms of surrogate models exist, but most rely on an initial dataset that spans the model's design space. The choice of points to appropriately cover the design space is key for all surrogate models, especially because often one does not know the critical regions of the design space before constructing the dataset. An alternative to the aforementioned methods for determining hydrodynamic coefficients and derivatives, is to develop a surrogate model based on data from many BEM simulations of similar structures and use this surrogate model to predict hydrodynamic coefficients and their derivatives. In this context, the hydrodynamic coefficients are frequency-dependent excitation forces (diffraction and Froude–Krylov forces), added mass and radiation damping.

Several challenges exist with applying surrogate modeling techniques to a BEM solver. The main challenge is that surrogate models perform best when a model has relatively few inputs. As the number of inputs increases, many more sampling points are needed to ensure coverage of the design space. This is referred to as 'the curse of dimensionality' (Martins and Ning, 2021, Chapter 10). The main input for a BEM solver is a mesh of panels, however typical meshes have hundreds to thousands of panels, each with several properties. Instead, a surrogate model must be built around a combination of a

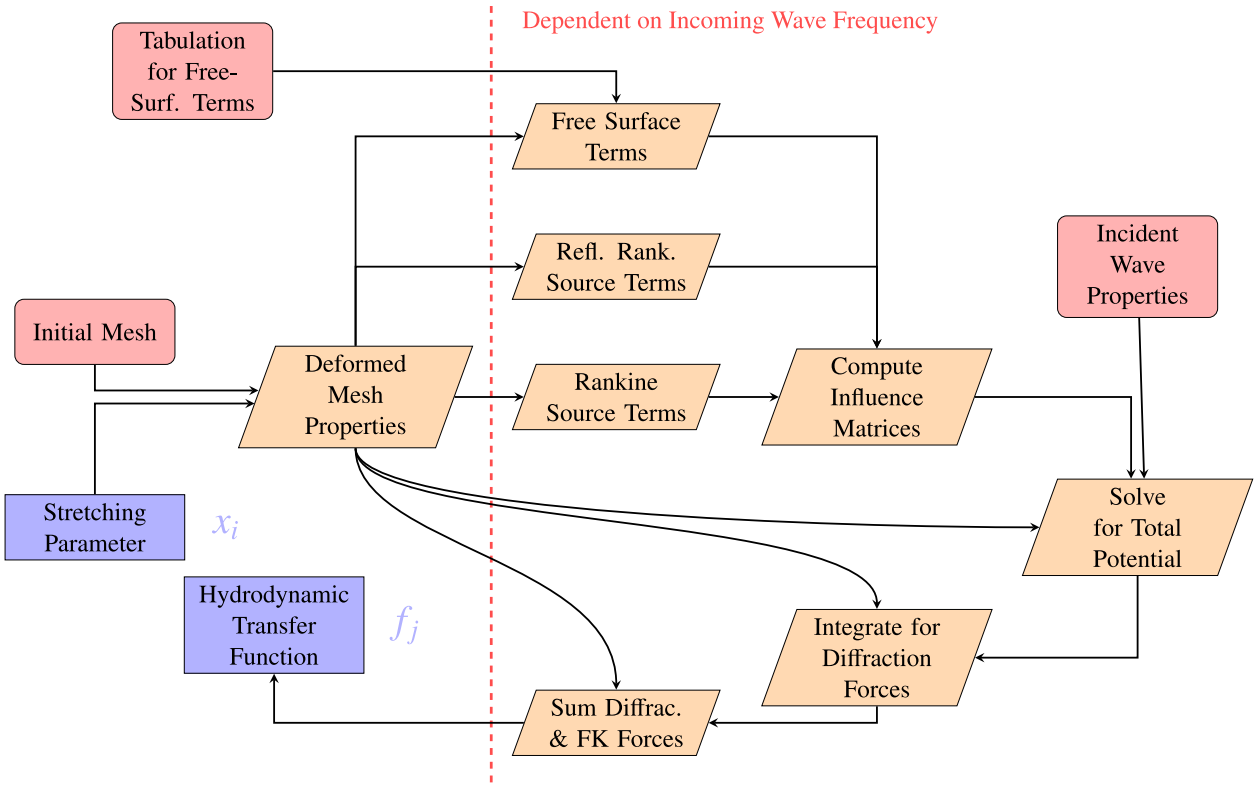

Fig. 3. Flowchart of differentiated boundary element method solver for the diffraction problem. The total derivative $\frac{df_j}{dx_i}$ of a hydrodynamic transfer function with respect to a stretching parameter is computed.

mesh generation tool with relatively few ($\mathcal{O}(10)$) variables and a BEM solver. This means that each new structure concept considered requires a new training dataset be generated. Furthermore, the BEM solution is frequency-dependent, so the surrogate model must either be able to predict the entire frequency range, or separate surrogate models must be developed for each wave frequency of interest.

3. Methodology

In this work, computation of radiation and diffraction forces and their analytical gradients has been achieved by modifying the open-source BEM solver Capytaine (Ancellin and Dias, 2019), which is based on another open-source BEM solver, NEMOH (Babarit and Delhommeau, 2015; Kurnia and Ducrozet, 2023). The new differentiated boundary element method solver, DBEMS, is implemented using the OpenMDAO framework (Gray et al., 2019) to allow for definition of gradients and integration into optimization models in the future.

A flowchart of the solver methodology for the diffraction problem is presented in Fig. 3. Derivatives are computed for the outputs (hydrodynamic transfer functions) with respect to the inputs (mesh stretching parameters) both shown in blue boxes. The red boxes indicate parameters that are fixed or outside the total derivative computation, meaning partial derivatives are not computed for these terms. The orange trapezoids indicate processes in DBEMS, i.e. pieces of the solver that have exact partial derivatives defined. All blocks to the right of the dashed red line are dependent on the incoming wave frequency, meaning they must be run for each wave frequency of interest. A similar methodology is used for the radiation problem. For the radiation problem, the hydrodynamic transfer functions are frequency-dependent added mass and radiation damping and there is no summation with Froude–Krylov (FK) forces.

While DBEMS follows the design of other open-source BEM solvers, Section 3.1 describes the details of the solution method that are relevant for developing a differentiated solver. The generation of the mesh used by DBEMS and deformation methods are described in Section 3.1.1. To enable differentiation with respect to geometric parameters, mesh deformation is included within DBEMS as illustrated in Fig. 3. The specific changes to a 'standard' BEM solver that have been necessary to compute analytic derivatives are described in Section 3.2.

3.1. Design of boundary element solver

DBEMS is based heavily on Capytaine (Ancellin and Dias, 2019), which relies on routines for computation of the Green function from NEMOH (Babarit and Delhommeau, 2015; Kurnia and Ducrozet, 2023). An overview of the layout of the solver is given in Fig. 4. Given a mesh, a specific wave frequency, and a water depth, influence matrices are constructed. These influence matrices contain the coefficients of an approximation, Eq. (20), of the potential on the body and its gradient, expressed in Eqs. (10) and (11).

$$\Phi = S\sigma, \quad u = K\sigma \tag{20}$$

The K influence matrix forms a linear system of equations with the unknown source distribution on the body and the known normal velocity on the body. The potential distribution on the body is then calculated as a product of the S influence matrix and the source distribution. From the potential distribution on the body, pressure can be easily computed. Excitation forces, added mass, and radiation damping can be computed by integrating the pressure distribution over the body surface.

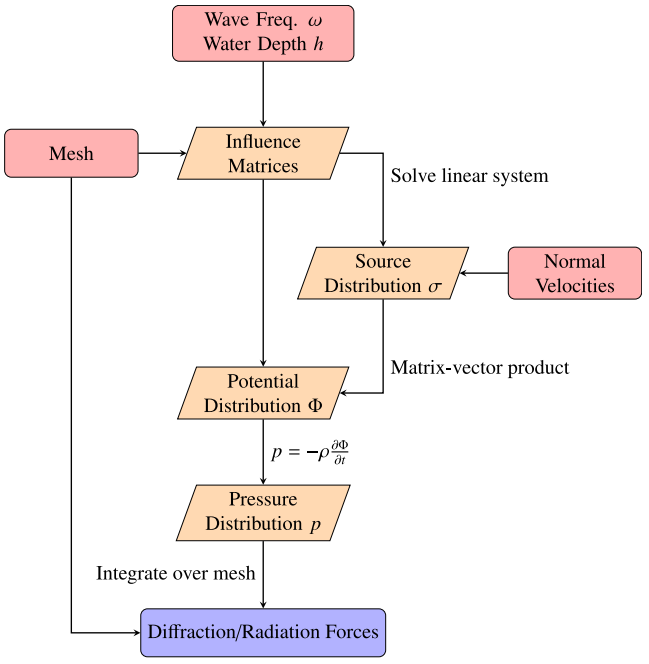

Fig. 4. Flow of boundary element method solver.

3.1.1. Mesh generation

The main input to a BEM solver for diffraction and radiation forces is a mesh describing the body of interest. The mesh consists of panels, typically quadrilaterals, that are a discretization of the body surface. For complex structures, developing the mesh based on three-dimensional geometry can be a considerable effort. Several software tools exist that generalize this process, though none can provide derivatives with respect to input sizing parameters to the authors' knowledge. To avoid the significant implementation required to develop such a tool, DBEMS requires an initial mesh layout that is not a design variable. This initial mesh represents a baseline design and allows for consistent definition of stretching or deformation parameters that are specific to each architecture (single column, multi-column, etc.) considered. The initial mesh can be generated by any available tool, and the inputs to the differentiated boundary element solver are the locations of each vertex on the mesh, a mapping of vertices to panels, and a mapping between the vertices and the stretching parameters, the design variables with respect to which derivatives are taken. Stretching is applied directly to the mesh, rather than the body geometry. This method of starting with an initial mesh and stretching follows similar tools like PyGeo (Hajdik et al., 2023) which implements the free-form deformation (FFD) approach, though DBEMS stretches the geometry of the mesh itself rather than an enclosing form as in FFD. The advantage of approaches like FFD and the present approach is that rather than developing a full parametric geometry which would include many design variables of limited relevance, only the stretching parameters are included, vastly reducing the number of design variables needed (Kenway et al., 2010).

Each mesh panel is defined by four vertices. Based on these four vertices, the panel center, normal vector (into the fluid) at the panel center, panel area, and maximum radius from panel center to panel nodes can be computed. Because the location of mesh vertices is modified by the stretching parameters, all of these functions are defined with derivatives. Changes to the mesh inside an optimization loop therefore require re-computation of all mesh parameters, however the panel arrangement – which vertices comprise each panel – remains constant.

Integration of the Green function and excitation forces uses a single-point quadrature based only on the panel center location and the panel area. Non-dimensional distances used for computing terms in the influence matrices are also computed based only on panel centers.

3.1.2. Computation of influence matrices

The influence matrices in Eq. (20) represent the discretization of the integral of the Green function and the integral of the gradient of the Green function. The velocity potential is assumed to be constant over the entire surface of each panel, and is represented by a point at the panel center. The S influence matrix contains the integrals of the Green function, given in Eq. (21a), while the K influence matrix contains the integrals of the gradients of the Green function, given in Eq. (21b). The delta function (δ_{nm}) is equal to one if $n = m$ and zero otherwise. Constant coefficients are omitted here for clarity.

$$S_{nm} = \iint_{\Gamma_i} G(\boldsymbol{x_i};\boldsymbol{\xi})\mathrm{d}S(\boldsymbol{\xi}) \tag{21a}$$

$$K_{nm} = \frac{\delta_{nm}}{2} + \iint_{\Gamma_i} \nabla_x G(\boldsymbol{x_i};\boldsymbol{\xi})\cdot n_i \mathrm{d}S(\boldsymbol{\xi}) \tag{21b}$$

As discussed in Section 2.1.1, the Green function consists of three main components: a Rankine source term, a reflected Rankine source term, and a free surface term. For this work, a form of the Green function from Babarit and Delhommeau (2015) is used as given in Eq. (22). In this form, the Green function gives the velocity potential at a point $M(x, y, z)$ due to a source at the point $M'(x', y', z')$. MM' is equivalent to r in Eq. (7) and $MM^{0\prime}$ is equivalent to r' where $M^{0\prime}$ is the point reflected over the free surface. The function $J(\zeta)$ is defined in Eq. (23) using the exponential integral E_1 (Eq. (24)) where $\zeta = k(z+z'+ir\cos\theta)$, and $r = \sqrt{(x-x')^2+(y-y')^2}$.

$$\begin{aligned} G(M,M') = {} & \frac{1}{MM'} - \frac{1}{MM^{0\prime}} \\ & + 2k\left[\frac{1}{\pi}\mathrm{Re}\int_{-\pi/2}^{\pi/2}\left(J(\zeta)-\frac{1}{\zeta}\right)d\theta \right. \\ & \left. + i\mathrm{Re}\int_{-\pi/2}^{\pi/2} e^{\zeta}d\theta\right] \end{aligned} \tag{22}$$

$$J(\zeta) = \begin{cases} e^{\zeta}(E_1(\zeta)+i\pi) & \text{if } \mathrm{Im}(\zeta)\geq 0 \\ e^{\zeta}(E_1(\zeta)-i\pi) & \text{if } \mathrm{Im}(\zeta)<0 \end{cases} \tag{23}$$

$$E_1(\zeta) = \int_{\zeta}^{\infty}\frac{e^{-t}}{t}dt \tag{24}$$

The Green function given in Eq. (22) can be re-written as a sum of three parts, as in Eq. (25), where G^0 is the Rankine source term, G^1 is the reflected Rankine source term, and G^2 is the free surface term. Similarly the expressions for each entry in the influence matrices (Eqs. (21a) and (21b)) can be rewritten as a sum of three terms as in Eqs. (26a) and (26b), now shown with constant coefficients.

$$G(M,M') = G^0(M,M') - G^1(M,M') + G^2(M,M') \tag{25}$$

$$S_{nm} = -\frac{1}{4\pi}\left(S^0_{nm} - S^1_{nm} + S^2_{nm}\right) \tag{26a}$$

$$K_{nm} = -\frac{1}{4\pi}\left(K^0_{nm} - K^1_{nm} + K^2_{nm}\right) + \frac{\delta_{nm}}{2} \tag{26b}$$

Based on the existing open source BEM solvers Capytaine (Ancellin and Dias, 2019) and NEMOH (Babarit and Delhommeau, 2015), an analytical expression is used for the Rankine terms, while the free surface term is based on interpolation. The expressions for the Rankine terms (S^0_{nm} and K^0_{nm}) and reflected Rankine terms (S^1_{nm} and K^1_{nm}) are given in Eqs. (27a), (27b), (28a) and (28b) respectively following Babarit and Delhommeau (2015). Here the influence from panel m with center at M' on panel n with center at O_n is computed, the O_nM' term is equivalent to r. The free surface terms (S^2_{nm} and K^2_{nm}) given in Eqs. (29a) and (29b) have no closed-form analytic expression. Computation of these follows work by Delhommeau (1989) and is based on interpolation in

pre-computed tabulated functions. This is discussed in more detail in Section 3.2.2.

$$S^0_{nm} = \iint_{\Sigma_m} \frac{1}{O_n M'} dS' \tag{27a}$$

$$K^0_{nm} = \iint_{\Sigma_m} \frac{\partial}{\partial n}\left(\frac{1}{O_n M'}\right) dS' \tag{27b}$$

$$S^1_{nm} = -\iint_{\Sigma_m} \frac{1}{O_n M^{0\prime}} dS' \tag{28a}$$

$$K^1_{nm} = -\iint_{\Sigma_m} \frac{\partial}{\partial n}\left(\frac{1}{O_n M^{0\prime}}\right) dS' \tag{28b}$$

$$S^2_{nm} = 2k\mathrm{Re}\int_{-\pi/2}^{\pi/2}\left[\frac{1}{\pi}\iint_{\Sigma_m}\left(J(\zeta) - \frac{1}{\zeta}\right)dS' + i\iint_{\Sigma_m} e^{\zeta} dS'\right] d\theta \tag{29a}$$

$$K^2_{nm} = 2k\mathrm{Re}\int_{-\pi/2}^{\pi/2}\left[\frac{1}{\pi}\frac{\partial}{\partial n}\iint_{\Sigma_m}\left(J(\zeta) - \frac{1}{\zeta}\right)dS' + i\frac{\partial}{\partial n}\iint_{\Sigma_m} e^{\zeta} dS'\right] d\theta \tag{29b}$$

3.1.3. Symmetry

Physical symmetry of the body can be exploited to reduce computational cost because the wave source potential and its gradient (Eqs. (10) and (11)) have a symmetric and anti-symmetric pattern corresponding to physical symmetry. Therefore, for a given body with two planes of symmetry, the body can be modeled with only one quarter of the panels. The resulting influence matrices have the same rank as if physical symmetry was not considered, but the block Toeplitz structure of these matrices means the linear system representing source distribution in Eq. (20) can be solved more efficiently. The block Toeplitz structure is nested at the 'top level' meaning that for a body with $4N$ panels, the linear system can be solved with two system solves of rank $2N$. The matrix–vector product in Eq. (20) is computed with the full rank $4N$ matrix.

3.1.4. Radiation capability

For diffraction forces, a single linear system solve is needed where the normal velocity on the body is zero. For radiation forces (frequency-dependent added mass and damping), several solves are needed where the normal velocity on the body is given for each degree of freedom. For the standard six degrees of freedom, this leads to 6 system solves. The computational cost of this solution can be slightly reduced with a solver based on the LU decomposition method, however the computational cost is still greater than for diffraction forces.

3.2. Modifications for gradients

A number of modifications are necessary to the 'standard' boundary element method solver workflow to include calculation of analytic gradients. The procedure as described in Section 3.1 has been implemented in the OpenMDAO framework (Gray et al., 2019) so that the model can be evaluated with implicit analytic total derivatives. Both the direct or adjoint method are implemented for solving the total derivatives depending on the number of design variables and outputs. The procedure is divided into several groups of components, where each component includes a portion of the overall model and exact partial derivatives of that portion. The components are chosen in such a way to make definition of these exact partial derivatives possible, and where relevant partial derivatives are defined using sparse matrices.

3.2.1. Constant mesh paneling

To preserve analytic differentiability, the size of the constituent matrices in the problem must remain constant, meaning the number and arrangement of panels in the body mesh must be held constant. For calculation of gradients of forcing with respect to deformation variables on the initial mesh, this is not problematic. In optimization, however, deformed designs will have a different mesh resolution. The impact is believed to be minor for relatively small deformations, provided panels remain small enough to capture the key wave frequency range. In the context of design optimization for floating structures, deformations are expected to be small as large deformations would lead to significant changes in displacement and mass of the structure.

3.2.2. Expanded tabulation for free surface Green function

The free surface term of the influence matrices (based on the free surface term in the Green function, $G^2(M, M')$ in Section 3.1.2) is computed for each panel pair based on interpolation. This is possible because the free surface terms, Eqs. (29a) and (29b), can be expressed as a sum of functions depending only on the non-dimensional distances, Z and X. These functions are given in Eqs. (30a)–(30d) from Babarit and Delhommeau (2015).

$$D_1(Z, X) = \mathrm{Re}\left[\int_{-\frac{\pi}{2}}^{\frac{\pi}{2}} (-i\cos\theta)(J(\zeta) - \frac{1}{\zeta}) d\theta\right] \tag{30a}$$

$$D_2(Z, X) = \mathrm{Re}\left[\int_{-\frac{\pi}{2}}^{\frac{\pi}{2}} (-i\cos\theta) e^{\zeta} d\theta\right] \tag{30b}$$

$$Z_1(Z, X) = \mathrm{Re}\left[\int_{-\frac{\pi}{2}}^{\frac{\pi}{2}} (J(\zeta) - \frac{1}{\zeta}) d\theta\right] \tag{30c}$$

$$Z_2(Z, X) = \mathrm{Re}\left[\int_{-\frac{\pi}{2}}^{\frac{\pi}{2}} e^{\zeta} d\theta\right] \tag{30d}$$

In Capytaine and NEMOH, an asymptotic approximation of these functions is used for large values of the non-dimensional variables (large panel-to-panel distances) and interpolation on a pre-computed tabulation is used for smaller values of these non-dimensional variables, 'near' panels. This approach is not differentiable due to the conditional logic, so in this work only the tabulation is used. To ensure that all possible non-dimensional variables are included in the tabulation, tabulated values are computed for an expanded range of non-dimensional variables based on the initial mesh. This has minimal additional computational cost, as the functions can be evaluated a single time, outside any optimization loop. Because the tabulated values do not change as the mesh changes, derivatives of these functions are not necessary to find total derivatives of wave excitation or radiation terms. For efficiency, the original Fortran functions from Capytaine are used to compute these functions.

In NEMOH and Capytaine, as described in Babarit and Delhommeau (2015), the interpolation of these functions uses a fifth-order Lagrange polynomial surface based on the nearest-index for a given point. In this work, a second-order Lagrange polynomial interpolation over the fixed, pre-calculated two-dimensional table provides function values and derivatives of these values with respect to the non-dimensional inputs. This reduction in order of the interpolation has not been shown to cause any issues with accuracy for the cases considered. In most cases, the reduced-order interpolation is within approximately 0.1% of the interpolation used in Capytaine. The pre-computed functions (Eqs. (30a)–(30d)) are sensitive to small changes in Z and X near zero, so appropriate spacing of points in the tabulation and accurate interpolation are important.

3.2.3. Linear system solve

A built-in linear system solver from the OpenMDAO framework is used to solve the linear system in Eq. (20). This implicit solver implements the LU decomposition method and defines exact partial derivatives. Because the OpenMDAO framework requires all component

Table 1
Summary of the forcing and derivative methods applied in the present work.

Name	Forcing method	Derivative method	Single column	Multiple column
WAMIT	Commercial BEM solver	None	✓[a]	✓[b]
FK	Froude–Krylov forces only	None	✓	✓
MACF	MacCamy–Fuchs and Froude–Krylov forces	Implicit analytic[c]	✓	
MOJS	Morison-type forces and Froude–Krylov forces	Implicit analytic[c]		✓
SURR	Response surface surrogate model[d]	Implicit analytic[c]		✓
DBEMS	Differentiated BEM solver	Implicit analytic[c]	✓	✓
FD	DBEMS	Finite difference[e]	✓	✓

[a] Exact geometry using higher-order method with irregular frequency removal.
[b] High-resolution mesh using low-order with irregular frequency removal.
[c] Implicit analytic total derivatives based on exact partial derivatives. Single column results using direct method and multiple column results using adjoint method.
[d] Response surface model based on least-squares regression of 9600 samples. See details in Section 4.2.1.
[e] Forward finite differences with step size of 1×10^{-6}.

inputs and outputs be real-valued, each complex linear system $\left(\tilde{A}\tilde{x} = \tilde{b}\right)$ with rank N must be rewritten as a real-valued system with rank $2N$ as shown in Eq. (31).

$$[\tilde{A}] = \begin{bmatrix} A^{re} & -A^{im} \\ A^{im} & A^{re} \end{bmatrix}, \quad \vec{\tilde{b}} = \begin{bmatrix} b^{re} \\ b^{im} \end{bmatrix} \rightarrow \vec{\tilde{x}} = \begin{bmatrix} x^{re} \\ x^{im} \end{bmatrix} \tag{31}$$

3.2.4. Total derivative computation

Total derivatives, for example derivatives of wave excitation with respect to the mesh stretching parameters, are calculated using the implicit analytical method.

Each component in the model has exactly defined partial derivatives, computed using symbolic differentiation (see Martins and Ning, Chapter 6.3 (Martins and Ning, 2021)) or by hand. Components are further arranged into groups, and some groups employ solvers to ensure group-level convergence. Because the boundary element method solution is valid for a single frequency, several solvers can be run in parallel based on the same mesh parameters. This produces a heterogeneous hierarchy, where different 'levels' of solvers are applied to different parts of the model as needed and both explicit and implicit components can be mixed. The MAUD architecture, developed by Hwang and Martins (2018), is applied in OpenMDAO to efficiently solve the coupled systems with heterogeneous solver hierarchy and compute the total coupled derivatives.

4. Results and discussion

Two case studies have been conducted to demonstrate the capability and accuracy of the method developed in this work. The first case study considered a single floating circular cylinder with constant diameter. For this very simple example, forcing results in the horizontal direction can be compared to the analytical solution developed by MacCamy and Fuchs, which can be exactly differentiated. The second case study considered a large volume structure with three in-line square columns connected to a horizontal rectangular pontoon. This example provides a relatively simple case when existing empirical and analytical solutions (Morison' equation, MacCamy–Fuchs theory) perform poorly. There are no existing methods that can provide accurate derivatives of the excitation loads for this example. For both case studies, diffraction forces and derivatives of these forces with respect to stretching parameters are presented. For the multiple column case, added mass and radiation damping results are also presented. A summary of the forcing and derivative methods used for each case study is given in Table 1.

Both case studies considered infinite water depth and incident wave frequencies from $0.01\,\mathrm{rad\,s^{-1}}$ to $2.1\,\mathrm{rad\,s^{-1}}$ (0.0016 Hz to 0.334 Hz) or incident wave periods from 2.99 s to 628.3 s.

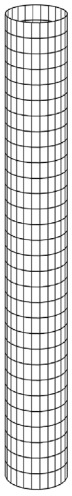

Fig. 5. Mesh considered for single column forcing.

4.1. Single column case study

The single column case study considered a right circular cylinder with a draft of 15 m and diameter of 2 m. The rigid cylinder extended to the free-surface and was fixed at the origin. Eleven stretching parameters were used, ten for the column radius and one for the total column draft. A spline was fit to the ten radius control points to find the radius stretch at each panel vertex or section.

As shown in Fig. 5, the mesh used with the differentiated boundary element method solver consisted of a total of 840 panels (210 panels in one quadrant with double symmetry) with 30 panels along the length of the spar and 24 panels around each circumference. The average panel area was $0.116\,\mathrm{m^2}$ and average panel radius was 0.261 m. DNV RP-C205 (DNV GL, 2014) recommends that a boundary element method mesh should have a fine enough resolution so that there are a minimum of six panels diagonally for the shortest wave considered. Based this recommended practice, the results for this mesh are valid up to an incident wave frequency of $1.77\,\mathrm{rad\,s^{-1}}$.

Analytic results using MacCamy–Fuchs theory were computed using 96 sections evenly distributed along the cylinder so each section had a vertical height of 0.156 m. To include forces in the heave direction, a Froude–Krylov force term was added to these results using a single dynamic pressure at the center of the cylinder's base and the area of the entire cylinder base. For reference results using WAMIT the 'higher-order' method using exact geometry was used including more wave frequencies (43 frequencies instead of 24).

Computing diffraction forces for the mesh used in this case study at 24 wave frequencies required 206.3 s using 8 cores (the 24 wave

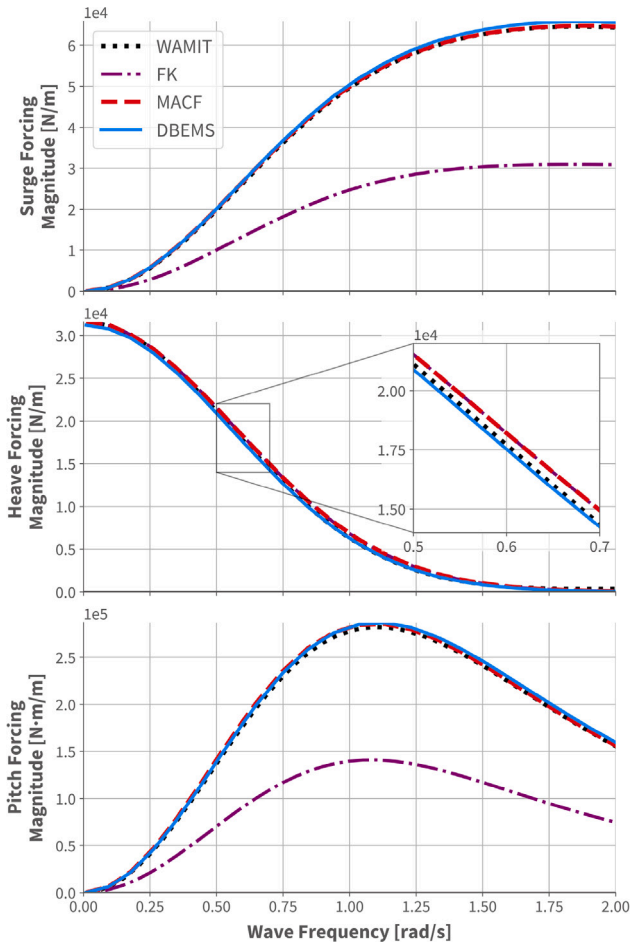

Fig. 6. Hydrodynamic transfer function verification for spar-type platform in selected modes.

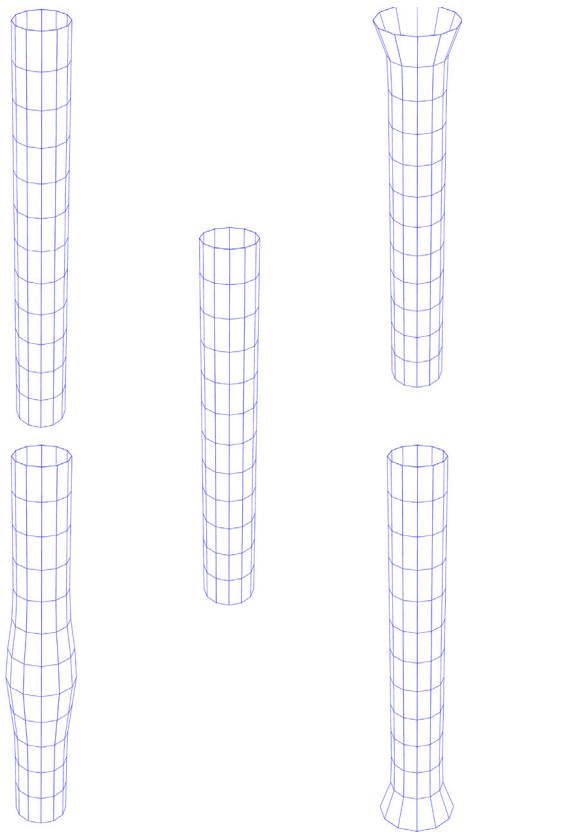

Fig. 7. Illustrations of stretching of single column mesh (clockwise from top left): column draft (1) and column radius at the free surface (2), middle (3), and base (4) of the column. Unstretched mesh shown in center.

frequencies were split into three runs) and 115.6 GB of memory. Computing implicit analytic total derivatives required an additional 375.8 s and 10.2 GB of memory, while computing finite difference total derivatives (based on the DBEMS forcing model) required an additional 383.1 s and 21.5 GB of memory. For reference, using Capytaine the forces (with no possibility of derivative computation) can be computed in under one second using around 100 MB of memory. The very high computational cost of the diffraction forcing model alone can be attributed to the model setup required to allow for derivative computation and relatively inefficient programming of the current version of DBEMS. The analytical forcing results (MacCamy–Fuchs theory) were computed by the same model simultaneously, using negligible additional computational effort.

4.1.1. Forcing

A comparison of the hydrodynamic transfer functions (wave excitation) for rigid body motions surge, heave, and pitch is shown in Fig. 6. The reference results from WAMIT, pure Froude–Krylov forces computed using WAMIT, combined MacCamy–Fuchs/Froude–Krylov analytical solution, and forcing from DBEMS are plotted. Only the magnitude of the complex transfer functions is plotted, but similar agreement is seen for the phase angle.

The results show very good agreement between all three methods. DBEMS slightly over-predicts the transfer function magnitude at above 1.25 rad s^{-1} in surge and around 1 rad s^{-1} in pitch, likely due to the relatively coarse mesh at the free surface. The MacCamy–Fuchs/Froude–Krylov analytical solution slightly over-predicts the heave excitation due to limitations using only a Froude–Krylov force term in heave. This can been seen in the inset in Fig. 6, where the pure Froude–Krylov force can be seen to show the same over-prediction in heave forcing. The pure Froude–Krylov force poorly predicts surge and pitch forcing as expected.

4.1.2. Derivatives

A comparison of the total derivatives of the hydrodynamic transfer function magnitude in rigid body surge for four stretching parameters is shown in the two lower panels of Fig. 8 (the forcing magnitudes are reproduced in the upper part of the figure for easier reference). A similar comparison for rigid body pitch is shown in Fig. 9. Derivatives are computed only at the 24 wave evaluation frequencies, and not interpolated. Four total derivatives are shown, representing change in the surge or pitch transfer function magnitude due to stretching column draft (1) and column radius at the base (2), middle (3), and top (4) of the column. The stretching directions are shown in Fig. 7. The Jacobian has been scaled to correspond to the change in transfer function magnitude due to a one-meter stretch in the respective parameter. This scaling was applied to all methods of total derivative computation to provide a more familiar physical interpretation of the Jacobian.

The total derivatives presented for the analytical (combined MacCamy–Fuchs/Froude–Krylov) solution are computed using the implicit analytic method, with exact partial derivatives written for each component. Forward finite difference total derivatives with a constant step size of 1×10^{-7} are also included. The step size was chosen based on a step size study, though the results indicate that the best step size varies with wave frequency and total derivative of interest.

Overall, the derivatives show quite good agreement between the analytical solution, the differentiated boundary element method solver,

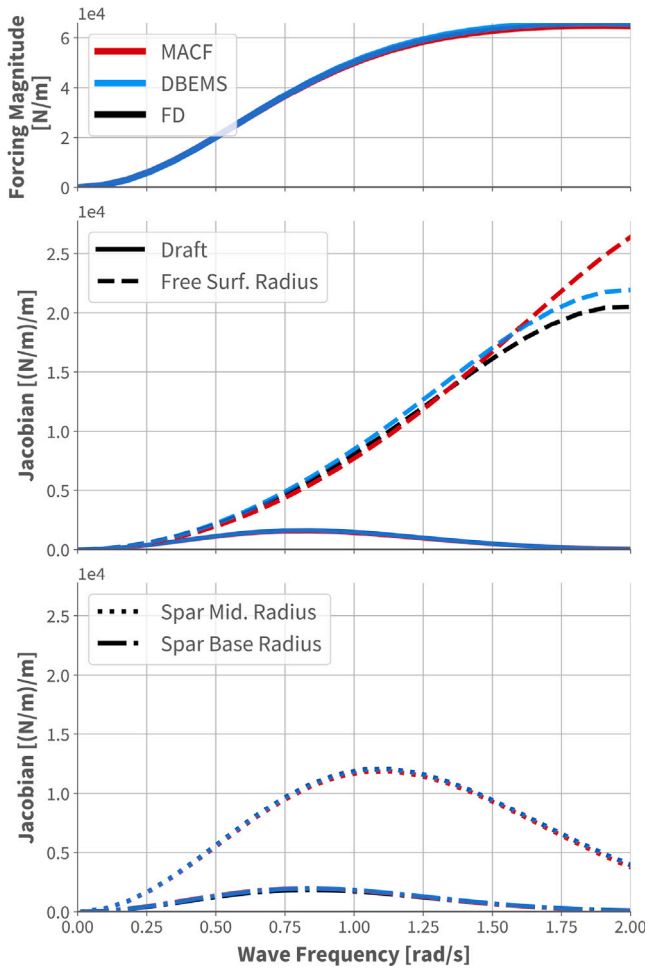

Fig. 8. Hydrodynamic transfer function and selected total derivatives for single column platform in surge mode.

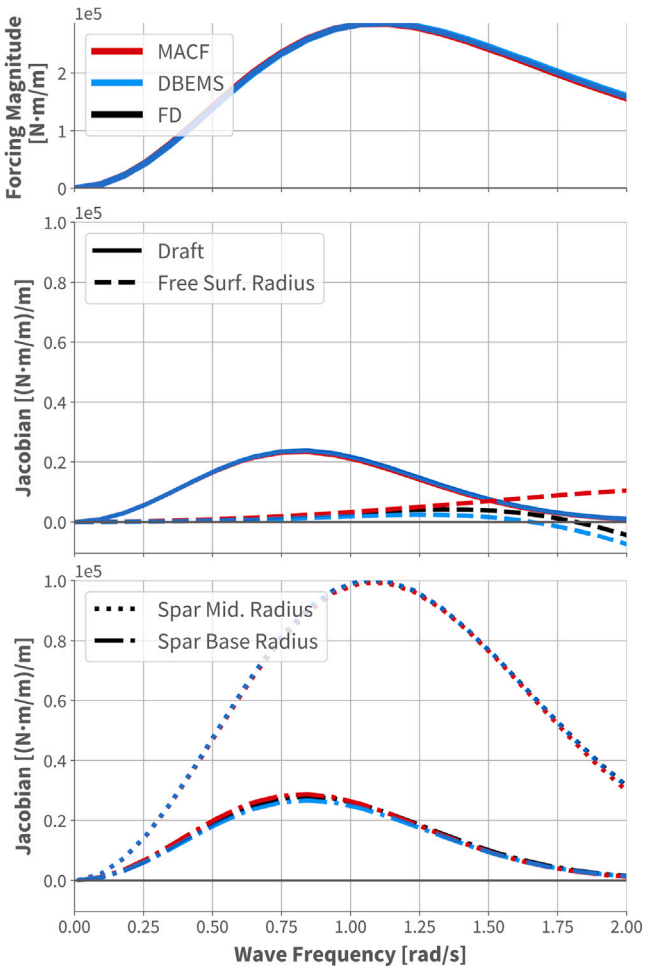

Fig. 9. Hydrodynamic transfer function and selected total derivatives for single column platform in pitch mode.

and finite differences. The results also follow intuition about how forcing is expected to change as a result of deformation. The surge total derivatives are largest for increases in radius at the center of the column at incident wave frequencies below $1.25\,\mathrm{rad\,s^{-1}}$ where diffraction forces are negligible for this structure, and largest for increases in radius at the free surface for higher frequencies. The pitch total derivatives are largest for increases in radius at the middle of the column, which is relatively near the free surface but has a larger moment arm to the origin of the coordinate system at the still water line.

The agreement between the three methods for total derivatives is worst for changes in radius at the free surface, especially at higher frequencies. Imperfect agreement between DBEMS and the finite difference approximation is likely due to a relatively coarse mesh at the free surface and greater sensitivity to the finite difference step size at higher incident wave frequencies. However the finite difference derivatives still show relatively good agreement with the DBEMS derivatives at the highest frequencies considered. The more significant differences between DBEMS and the analytical solution (MacCamy–Fuchs) can be explained by a difference in how radius stretching is treated in the two methods for computing forcing. As illustrated in Fig. 10, the MacCamy–Fuchs theory method considers sections of constant radius, while the panels in the mesh considered by the boundary element method solver have varying radius when the vertices are stretched. This difference is most pronounced at the free surface, where the incident wave potential is strongest.

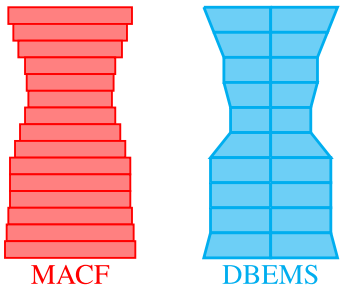

Fig. 10. Difference in radius stretching between MacCamy–Fuchs theory and DBEMS.

4.2. Multiple column case study

The multiple column case study considered a hypothetical rigid floating structure with three in-line square columns connected to a fully-submerged horizontal rectangular pontoon (Fig. 11). For the baseline design, the columns had a side length of 4 m and the total draft of the structure was 8 m. The distance from the free surface to the top of the pontoon was 6 m, and the distance between the center of each column was 24 m. The columns are in-line with the incoming wave direction so that column shadowing and interaction effects are relevant. While this structure does not resemble any known concept for floating structures, it provides an example with critical hydrodynamic interaction and is poorly suited for existing empirical or analytical

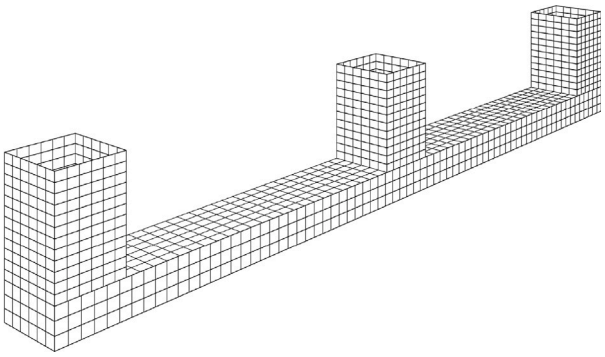

Fig. 11. Mesh considered for multiple column forcing.

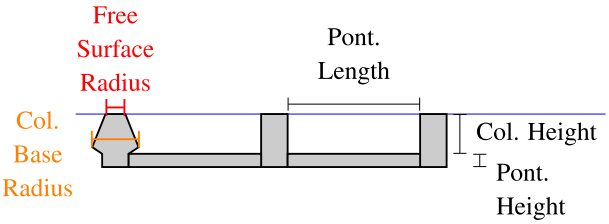

Fig. 12. Stretching parameters for multiple column case study. Pontoon width stretching is into the page and omitted from the figure.

Fig. 13. The MOJS model for the multiple column case study consists of five Morison-type components, three columns (red) and two horizontal submerged pontoons (blue).

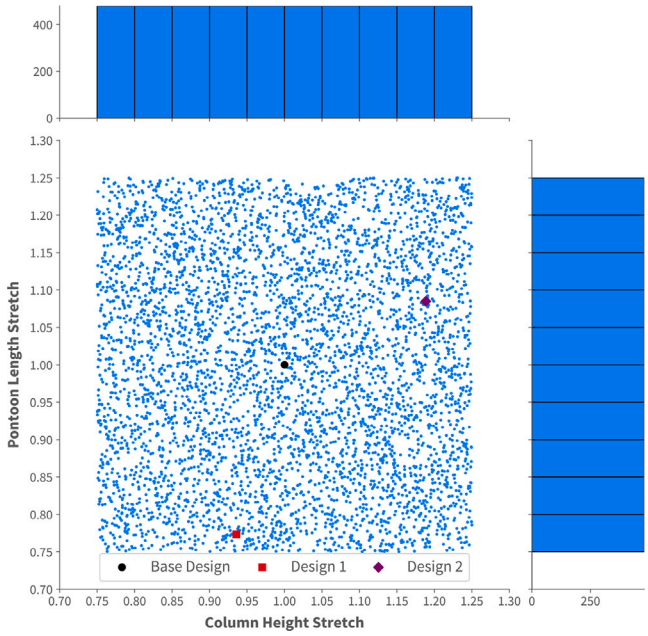

Fig. 14. Scatter plot and histograms of two design variables in surrogate model training dataset.

approaches. The structure can be accurately modeled with relatively few panels and is doubly-symmetric.

A total of 16 stretching parameters are defined for this case study, illustrated in Fig. 12. Six points control the radius of the outer two columns and six points control the radius of the central column. The radius of the square cross sections refers to the distance from the center of the square to each corner (half the diagonal length), or the radius of the circumscribed circle. Spline fitting is used to map the column radius control points to mesh vertices similar to the single column case study. Four scalar stretching parameters are defined for column height, pontoon height, pontoon width, and distance between columns.

The mesh used with the differentiated boundary element method solver consisted of a total of 2052 panels or 513 panels in one quadrant with double symmetry, The mesh used is shown in Fig. 11. The average panel area was 0.429 m^2 and average panel radius was 0.493 m, such that results should be valid up to an incident wave frequency of 1.29 rad s^{-1} (DNV GL, 2014).

An empirical forcing model was developed based on Morison's equation. A total of five components were modeled, the three vertical columns extending from the free surface to the total draft, and two horizontal pontoons between the columns as illustrated in Fig. 13. The coefficients used in Morison's equation based on the definition in Eqs. (12) and (13) are $C_M = 2.786$ and $C_D = 0$, as drag forces are not included in any of the other methods considered. To include heave forces on the vertical columns, a Froude–Krylov force term was added using a single dynamic pressure at the center of each column's base and the area of the column base. No end-effects on the pontoons were considered because they are coincident to the columns. Each column consisted of 40 sections, and each pontoon consisted of 20 sections.

Reference forcing results were developed using WAMIT's 'low-order' method which is roughly analogous to the method implemented in DBEMS, however the WAMIT results use a direct solver. In WAMIT, a much higher-resolution mesh (5860 panels) and 68 wave frequencies between 0.01 rad s^{-1} and 2.1 rad s^{-1} were used. Irregular frequency removal was applied as well, though no irregular frequencies were observed in the frequency range of interest.

Computing diffraction forces using the differentiated boundary element method solver at 24 wave frequencies required approximately 163 min (9828 s) and 75.3 GB of memory, as each wave frequency was computed separately. Computing implicit analytic total derivatives required an additional 137 min and 7.4 GB of memory, while computing finite difference total derivatives (based on the DBEMS forcing model) required an additional 393 min and 14.5 GB of memory. Forcing and total derivatives were computed for each wave frequency separately due to limits on the available computational resources, though computational time could be significantly reduced if all wave frequencies were run in parallel — provided a computer with enough memory was available. The surrogate model and empirical forcing models and their total derivatives were computed separately and required negligible computational resources, aside from surrogate model training data generation.

4.2.1. Surrogate model

A surrogate model was developed based on 9600 design variations of the baseline design using the same mesh as DBEMS with all stretching parameters ranging from 0.75 to 1.25. A Latin hypercube sampling approach was used to produce designs that evenly cover the design space, without any special consideration of how the stretching parameters affect results. Hydrodynamic coefficients were computed at 24 wave frequencies for each design using Capytaine (Ancellin and Dias, 2019) to correspond to the wave frequencies used by DBEMS. The same mesh used by DBEMS was used to develop the training data. Building this database of boundary element method results took approximately 29 h using a single core and roughly 8 GB of memory. An example of the distribution of the design variables in training data is given in Fig. 14, showing the random but even distribution over the design space.

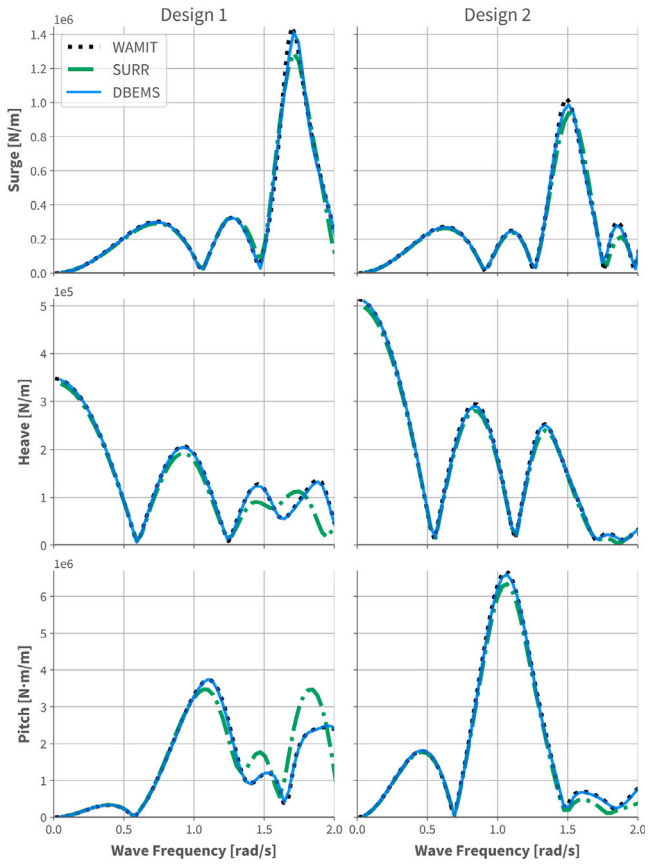

Fig. 15. DBEMS and surrogate model hydrodynamic transfer function verification for two random multiple column platform designs in selected modes.

Based on this database of results, a response surface surrogate model (implemented in OpenMDAO) was constructed with the stretching parameters as inputs and the hydrodynamic coefficients as outputs. The complex hydrodynamic coefficients were represented with two outputs — one real and one imaginary. The response surface surrogate model develops a second-order response surface for each model output using a least-squares solution to find the response surface equation coefficients. This is analogous to a least-squares regression model for each output. The response surface equation coefficients are generated during training, so evaluation of the response surface is very efficient and exact partial derivatives can be easily written. These exact partial derivatives can be used in implicit analytic total derivative computation. Once the database of training data was generated, training the surrogate model to generate response surface coefficients took roughly 40 s on a single core. Evaluation of the surrogate model, the only step that would be repeated in an optimization model, required less than one second.

Verification of the surrogate model was conducted for two random designs within in the design space, shown in the slice of the design space in Fig. 14. A comparison of the hydrodynamic transfer functions for wave excitation in rigid body surge, heave, and pitch for these two designs from WAMIT, the surrogate model, and DBEMS is shown in Fig. 15. Mean square error (MSE) for each design in each mode of response, using WAMIT results as the true values, is given in Table 2. The MSE is summed over all 24 wave frequencies and is nonzero for DBEMS due to the lower mesh resolution. Comparison of the MSEs shows that the surrogate model consistently has a larger error than DBEMS, but the performance of the surrogate is roughly equivalent across the design space. In Fig. 15 it can be seen the surrogate model performs worse at higher wave frequencies.

Table 2
Mean squared error of DBEMS and surrogate model forcing compared with WAMIT for three multiple column platform designs. Surge and heave MSE in units of N^2 and pitch MSE in units of $N^2\,m^2$.

Design	Mode	MSE DBEMS	MSE Surr.
Design 1	Surge	2.983×10^7	6.184×10^9
	Heave	3.532×10^6	8.894×10^8
	Pitch	6.100×10^8	5.395×10^{11}
Base Design	Surge	1.256×10^7	1.945×10^9
	Heave	1.174×10^7	1.033×10^8
	Pitch	4.131×10^9	4.606×10^{10}
Design 2	Surge	1.944×10^7	4.690×10^9
	Heave	8.820×10^6	9.409×10^7
	Pitch	3.300×10^9	4.585×10^{10}

4.2.2. Forcing

For the baseline three column design, a comparison of the hydrodynamic transfer functions (wave excitation) in rigid body surge, heave, and pitch is shown in Fig. 16. Both magnitude and phase angle (relative to the incident wave) of the complex transfer functions are plotted. The reference hydrodynamic transfer functions computed using WAMIT are plotted alongside a pure Froude–Krylov model, the empirical model, the surrogate model, and DBEMS. There are several cancellation frequencies observed (in contrast to the single column results in Fig. 6) showing the effects of interaction among the columns and pontoon.

The agreement between DBEMS and the reference WAMIT results is very good for all frequencies considered. Some slight differences are observed at peaks in transfer function magnitude and reversals in phase angle which can likely be attributed to the much lower mesh resolution used in DBEMS.

The empirical model agrees reasonably well with the reference results for surge excitation, but the agreement is much worse for heave and pitch excitation where both peak magnitudes and cancellation frequencies are not captured by the empirical model. Because of large-volume members and significant interaction between members, the structure is poorly suited for an approximation based on Morison's equation. When compared to the pure Froude–Krylov force, however, the empirical model shows improved performance in predicting cancellation and peak frequencies.

The surrogate model agrees quite well with the reference WAMIT results for all degrees of freedom, but slightly under-predicts forcing magnitude at peaks for frequencies over $1\,\mathrm{rad\,s^{-1}}$. The phase of excitation predicted by the surrogate model also disagrees with the WAMIT results for frequencies over $1.5\,\mathrm{rad\,s^{-1}}$. This is likely due to the increased sensitivity to small design changes at higher wave frequencies where shorter incident wavelengths mean small changes in geometry have a larger impact on forcing. Many of the challenges with surrogate models discussed in Section 2.3 also likely contribute.

4.2.3. Radiation

A comparison of frequency-dependent added mass and radiation damping in rigid body surge, heave, and pitch is shown in Fig. 17. Frequency-dependent added mass and radiation damping are determined by solving the radiation problems. The added mass or damping in each degree of freedom shown are due to motion in the same degree of freedom (the diagonal terms in the added mass or damping matrices) and for the non-negligible off-diagonal (coupling) terms in the surge-pitch degree of freedom as well. The reference results from WAMIT, the surrogate model results, and results using DBEMS are shown. Due to computational limits a lower resolution mesh with only 528 panels (valid up to an incident wave frequency of $0.87\,\mathrm{rad\,s^{-1}}$ (DNV GL, 2014)) was used to compute the DBEMS radiation results. The empirical model as developed does not have the capability to compute frequency-dependent added mass or damping. Similar results exist for the single column case but are not shown for brevity.

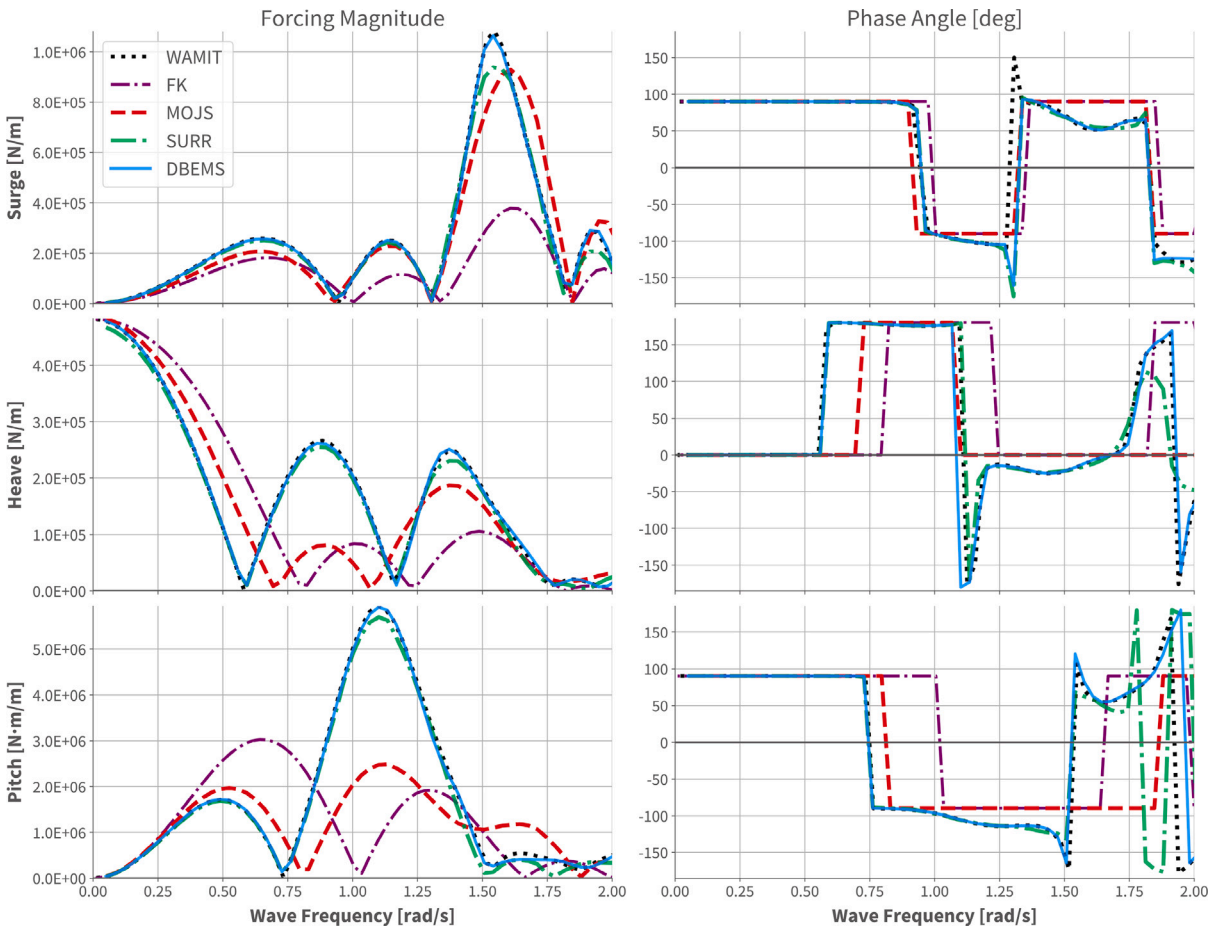

Fig. 16. Hydrodynamic transfer function verification for multiple column platform in selected modes.

Both added mass and radiation damping results agree very well for surge, heave, and pitch. The surrogate model again shows slightly worse agreement with reference results than DBEMS at frequencies over $1\,\mathrm{rad\,s^{-1}}$. This is likely due to the same causes for inaccuracy in the forcing results, most notably the increased sensitivity to small design changes at higher frequencies. Similar agreement is seen for the surge-pitch coupling terms. Computing the radiation forces that comprise added mass and radiation damping requires more computational time than the diffraction forces. The solution of the radiation problems does require solving more linear systems, though inefficiencies in model construction are believed to account for a bulk of the additional computational time required.

4.2.4. Derivatives

A comparison of the hydrodynamic transfer function magnitude for rigid body surge motion and total derivatives for three stretching parameters related to the vertical columns is shown in Fig. 18(a). A similar comparison for rigid body heave is shown in Fig. 18(b). A comparison of the hydrodynamic transfer function magnitude in rigid body surge and total derivatives for three stretching parameters related to the pontoon is shown in Fig. 19(a), and for heave in Fig. 19(b). Derivatives are computed only at the 24 wave evaluation frequencies, and not interpolated.

In all plots, transfer function magnitude is shown for the empirical (Morison's equation) model, the surrogate model, and DBEMS. Total derivatives computed using a forward finite difference method (using the DBEMS solver) are also included. The finite difference derivatives are the best comparison available for the derivatives from the differentiated boundary element method solver in the absence of existing analytic derivatives. The single column case study showed forward finite difference total derivatives with a step size of 1×10^{-7} generally agreed well with the analytical solution and DBEMS.

All total derivatives are taken with respect to the magnitude of the transfer function and again represent a portion of one column of the total Jacobian. The magnitude of the Jacobian has been scaled to correspond to the change in transfer function magnitude due to a one-meter stretch in the respective parameter.

Generally, analytic total derivatives from DBEMS agree well with the finite difference approximation of the derivatives. Notable exceptions to this agreement are seen at wave frequencies above $0.75\,\mathrm{rad\,s^{-1}}$ in stretching of the column base radius (just above the intersection with the pontoon) in both surge and heave excitation and at the column top (free surface) in surge excitation to a lesser extent. Both of these discrepancies are likely due to excessively coarse mesh resolution at the free surface and column/pontoon intersection — two regions that experience complex flow patterns. As an example, stretching the column base radius creates an overhanging geometry (shown in Fig. 12) that likely requires much higher panel resolution to resolve accurately. Agreement between the analytic total derivatives from DBEMS and finite difference approximation is also poor for stretching of the pontoon width above roughly $1\,\mathrm{rad\,s^{-1}}$, though this is more likely to due to the use of a constant finite difference step size of 1×10^{-7}.

The derivatives computed using the empirical model generally follow the sign and order of magnitude of the analytic and finite difference results from DBEMS but struggle to accurately capture the total derivatives due to inaccuracies in the underlying excitation prediction as discussed in Section 4.2. Discrepancies in the way that radius stretching is handled between the empirical and boundary element method model are similar to the single column results as illustrated in Fig. 10. Finally,

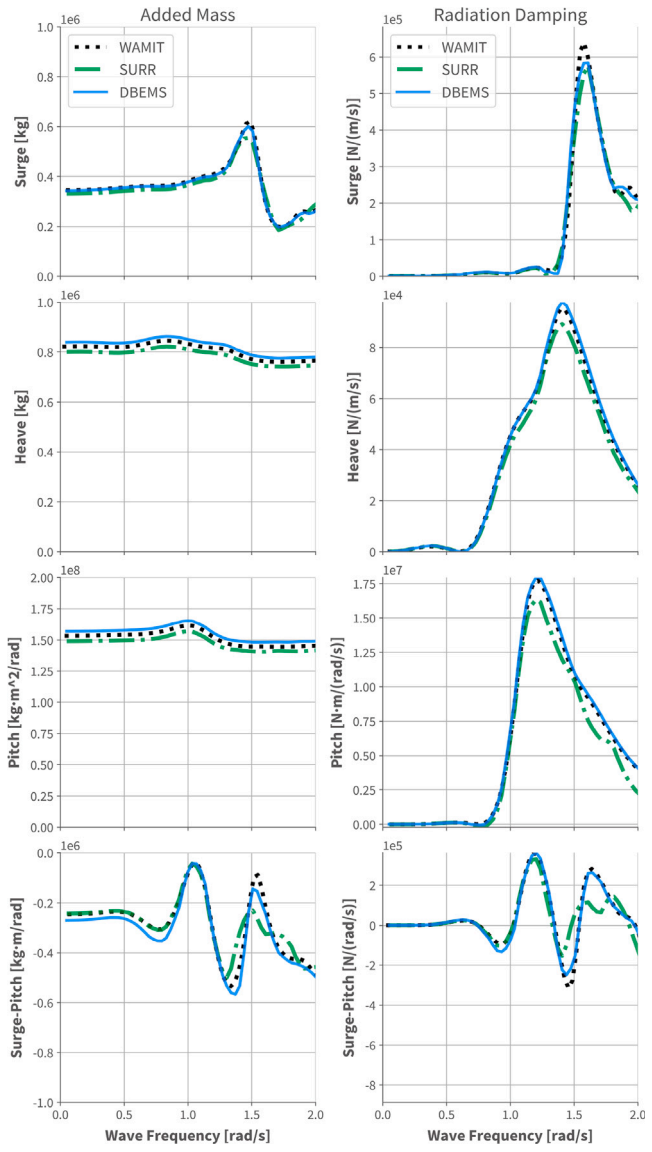

Fig. 17. Frequency-dependent added mass and radiation damping for multiple column platform in selected modes.

heave excitation for the columns is based solely on the base area, controlled by pontoon width rather than column radii, so the derivatives of heave excitation with respect to column radius are zero as expected.

The derivatives provided by the surrogate model agree quite well with the other methods for some parameters, but poorly for others. The surrogate model performs best for scalar parameters (all except the column radius stretching), and better for free surface radius stretching than column base radius stretching. Generally, the surrogate model derivatives are much closer to the other methods at lower frequencies, while at high frequencies the surrogate derivatives are noisy. This is consistent with existing literature on surrogate models for hydrodynamic coefficients which have seen high levels of noise in predictions (Kalimeris, 2023; Ilardi et al., 2024). The surrogate model derivatives do not out-perform the empirical model derivatives consistently at all frequencies (see surge force with respect to column base radius stretching for example) despite better forcing agreement with the reference results. Finite difference total derivatives were also computed for the surrogate model, and show excellent agreement with the analytic derivatives from surrogate model presented here. This suggests the discrepancies are due to noise in the surrogate model rather than how the derivatives are computed.

5. Conclusions

The results show that the differentiated boundary element method solver agrees with forcing and total derivative results in a verification case study (single column) with existing analytic total derivatives; and a case study (multiple column) not well captured by existing models — provided mesh resolution is adequate for the frequencies of interest.

The results also indicate several key limitations of the current model. For structures with complexity beyond the single column case study, there are few if any reliable methods for computing exact total derivatives to compare against. The comparisons presented in Section 4.2.4 therefore offer the best existing methods, and only the finite difference approximation agrees uniformly well with the analytic derivatives. More critically, DBEMS has very high requirements for computational resources — both CPU time and memory requirements. These computational requirements come in large part due to the inefficiency of the implementation, which must contain the total Jacobian matrix in memory to solve the linear system for analytic derivative computation. The method of separately running each wave frequency employed in the multiple column case study is not directly compatible with a full gradient-based optimization model.

Future work could focus on improvements to DBEMS as well as further development of the alternative models for determining diffraction and radiation forces and their derivatives. Performance improvements are believed to be achievable, for example by changing the programming language from Python to Fortran. In the current implementation functions are written in Python, with the exception of the integral calculation used to construct the tabulation used for the free surface term of the Green function (see Section 3.2.2), which is implemented in Fortran. The current implementation exploits physical symmetry of the body being considered, but does not make effective use of portions of the boundary element method solution that are symmetric (for example the Green function within each set of influence matrices) or portions that do not have a frequency-dependence and only need to be computed at a single wave frequency. Alternative boundary element method solvers could be built in a programming language with strong support for algorithmic differentiation, making derivative computation trivial.

None of the alternative methods for diffraction and radiation forces presented performed uniformly well in the current work, however further development work could improve this. In particular additional development of the surrogate modeling approach could provide a robust tool for computation of forces and derivatives. In addition to this work, the models presented by Zhang et al. (2020), Kalimeris (2023), and Ilardi et al. (2024) demonstrate that forcing prediction using surrogates is possible. Further work is still needed to apply surrogate models for forcing to gradient-based optimization models, particularly in reducing the noise in predictions which can lead to issues with optimizer convergence. Additional challenges include understanding uncertainty in the surrogate models, efficient generation of model training data, and balancing surrogate generality with accuracy. When considering diffraction and radiation loads for design optimization, the relative importance of these loads and the specific geometries being considered will determine which model for excitation loads and gradients is most applicable. For many concepts, an approach based on Morison/MacCamy–Fuchs/Froude–Krylov forces could perform reasonably well, as demonstrated by Alonso Reig et al. (2023) and in previous work by the authors Rohrer et al. (2023).

Based on the results of the two case studies, this work can be seen as a proof of concept for a differentiated boundary element method solver with analytic gradients. The excitation loads from the model agree well with reference results, and the total derivatives agree with the best available comparison data and make intuitive sense. The design of the solver allows for straightforward implementation in a future multidisciplinary design optimization model, though significant computational requirements pose a formidable challenge for widespread usage.

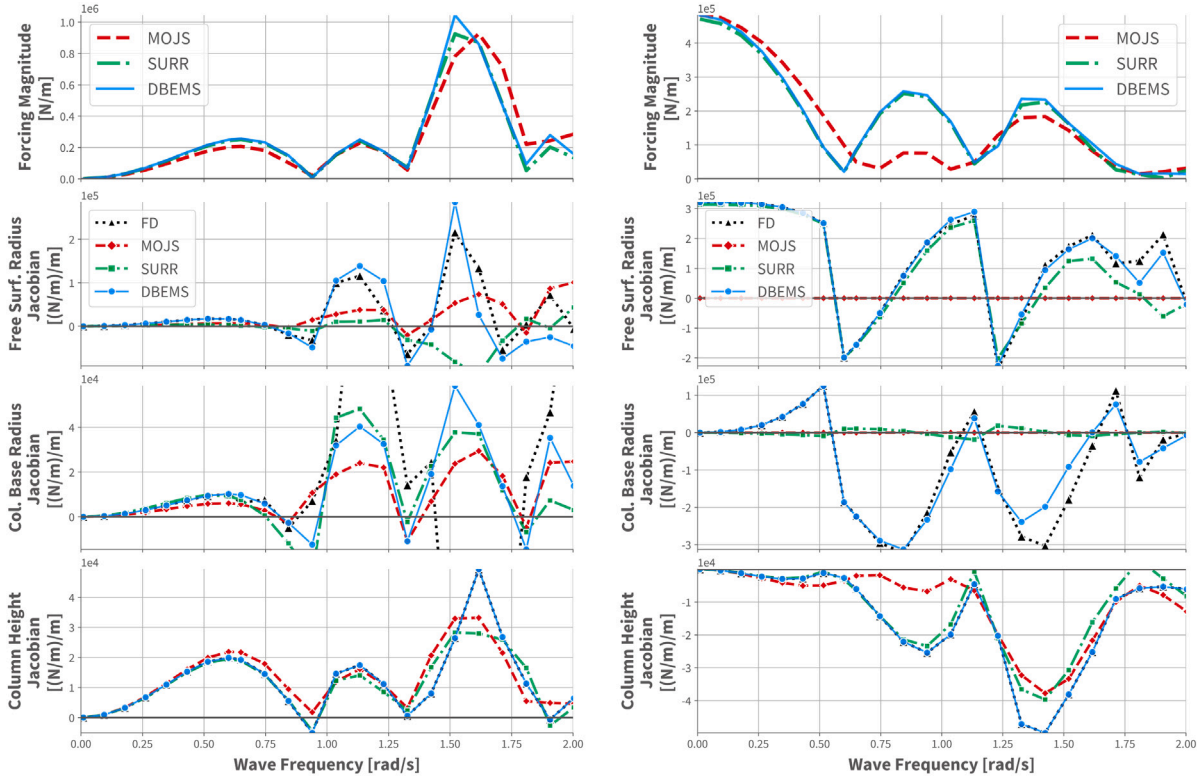

(a) Rigid body surge excitation.

(b) Rigid body heave excitation.

Fig. 18. Hydrodynamic transfer function and selected total derivatives related to column stretching for multiple column platform.

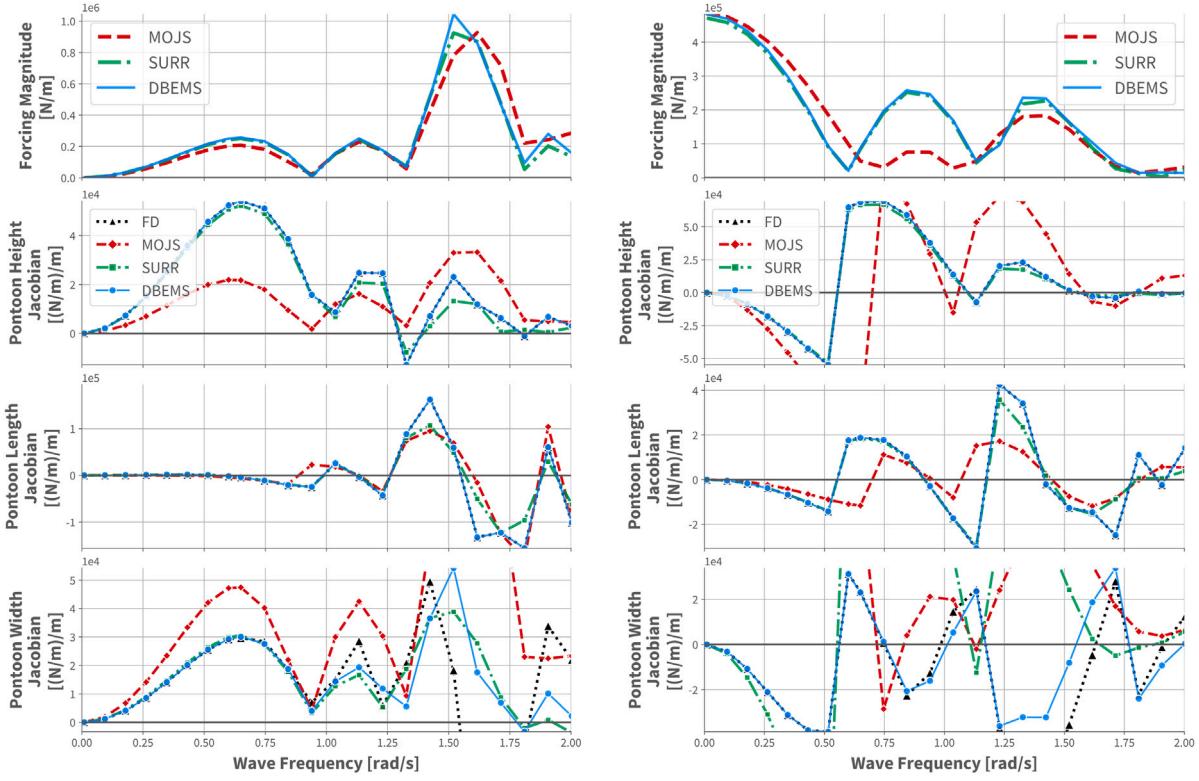

(a) Rigid body surge excitation.

(b) Rigid body heave excitation.

Fig. 19. Hydrodynamic transfer function and selected total derivatives related to pontoon stretching for multiple column platform.

CRediT authorship contribution statement

Peter J. Rohrer: Writing – review & editing, Writing – original draft, Visualization, Validation, Software, Methodology, Formal analysis, Conceptualization. **Erin E. Bachynski-Polić:** Writing – review & editing, Supervision, Project administration, Funding acquisition, Conceptualization.

Declaration of competing interest

The authors declare that they have no known competing financial interests or personal relationships that could have appeared to influence the work reported in this paper.

Data availability

Data will be made available on request.

Acknowledgments

The authors are grateful to John Marius Hegseth for thoughtful discussions and feedback through the development of this work. High-performance computing resources were provided by Sigma2 AS, through a Small Scale Exploratory Work provision.
Funding: This work was supported by the Research Council of Norway, through SFI BLUES, grant number 309281.

References

Alonso Reig, M., Mendikoa, I., Touzon, I., Petuya, V., 2023. Efficient hydrodynamic analysis for preliminary design of Floating Offshore Wind substructures. Ocean Eng. 285 (P1), 115318. http://dx.doi.org/10.1016/j.oceaneng.2023.115318.

Ancellin, M., Dias, F., 2019. Capytaine: a Python-based linear potential flow solver. J. Open Source Softw. 4 (36), 1341. http://dx.doi.org/10.21105/joss.01341.

Babarit, A., Delhommeau, G., 2015. Theoretical and numerical aspects of the open source BEM solver NEMOH. In: Proceedings of the 11th European Wave and Tidal Energy Conference. (EWTEC2015), Nantes, France, pp. 1–12.

Coe, R.G., Bacelli, G., Olson, S., Neary, V.S., Topper, M.B., 2020. Initial conceptual demonstration of control co-design for WEC optimization. J. Ocean Eng. Mar. Energy 6 (4), 441–449. http://dx.doi.org/10.1007/s40722-020-00181-9.

Delhommeau, G., 1989. Amélioration des perfomances des codes de calcul de diffraction radiation au premier ordre [Improvement of first order diffraction radiation computer codes]. In: 2èmes Journées de L'Hydrodynamique. Nantes, pp. 69–88.

DNV GL, 2014. DNV-RP-C205: Environmental conditions and environmental loads. Recommended Practice DNV-RP-C205.

Dou, S., Pegalajar-Jurado, A., Wang, S., Bredmose, H., Stolpe, M., 2020. Optimization of floating wind turbine support structures using frequency-domain analysis and analytical gradients. J. Phys. Conf. Ser. 1618 (4), http://dx.doi.org/10.1088/1742-6596/1618/4/042028.

Faltinsen, O.M., 1998. Sea Loads on Ships and Offshore Structures. Cambridge University Press.

Fylling, I., Berthelsen, P.A., 2011. WINDOPT: An optimization tool for floating support structures for deep water wind turbines. In: Ocean Space Utilization; Ocean Renewable Energy, vol. 5, ASMEDC, pp. 767–776. http://dx.doi.org/10.1115/OMAE2011-49985.

Garrett, C.J., 1971. Wave forces on a circular dock. J. Fluid Mech. 46 (1), 129–139. http://dx.doi.org/10.1017/S0022112071000430.

Gray, J.S., Hwang, J.T., Martins, J.R.R.A., Moore, K.T., Naylor, B.A., 2019. OpenMDAO: An open-source framework for multidisciplinary design, analysis, and optimization. Struct. Multidiscip. Optim. 59 (4), 1075–1104. http://dx.doi.org/10.1007/s00158-019-02211-z.

Hajdik, H.M., Yildirim, A., Wu, N., Brelje, B.J., Seraj, S., Mangano, M., Anibal, J.L., Jonsson, E., Adler, E.J., Mader, C.A., Kenway, G.K.W., Martins, J.R.R.A., 2023. pyGeo: A geometry package for multidisciplinary design optimization. J. Open Source Softw. 8 (87), 5319. http://dx.doi.org/10.21105/joss.05319.

Hall, M., Buckham, B., Crawford, C., 2014. Hydrodynamics-based floating wind turbine support platform optimization: A basis function approach. Renew. Energy 66, 559–569. http://dx.doi.org/10.1016/j.renene.2013.12.035.

Hegseth, J.M., Bachynski, E.E., Martins, J.R., 2020. Integrated design optimization of spar floating wind turbines. Mar. Struct. 72 (November 2019), 102771. http://dx.doi.org/10.1016/j.marstruc.2020.102771.

Hwang, J.T., Martins, J.R., 2018. A computational architecture for coupling heterogeneous numerical models and computing coupled derivatives. ACM Trans. Math. Software 44 (4), http://dx.doi.org/10.1145/3182393.

Ilardi, D., Kalikatzarakis, M., Oneto, L., Collu, M., Coraddu, A., 2024. Computationally aware surrogate models for the hydrodynamic response characterization of floating spar-type offshore wind turbine. IEEE Access 12 (October 2023), 6494–6517. http://dx.doi.org/10.1109/ACCESS.2023.3343874.

Kalimeris, T., 2023. Floating Wind Turbine Optimization Via Surrogate Modelling (Master's thesis). Norwegian University of Science and Technology and TU Delft.

Kenway, G.K., Kennedy, G.J., Martins, J.R., 2010. A CAD-free approach to high-fidelity aerostructural optimization. 13th AIAA/ISSMO Multidiscip. Anal. Optim. Conf. 2010 1–18. http://dx.doi.org/10.2514/6.2010-9231.

Kurnia, R., Ducrozet, G., 2023. NEMOH: Open-source boundary element solver for computation of first- and second-order hydrodynamic loads in the frequency domain. Comput. Phys. Comm. 292, 108885. http://dx.doi.org/10.1016/j.cpc.2023.108885.

Liao, Y., He, S., Martins, J.R., Young, Y.L., 2020. Hydrostructural optimization of generic composite hydrofoils. AIAA Scitech 2020 Forum 1 Part F, http://dx.doi.org/10.2514/6.2020-0164.

Liao, Y., Martins, J.R., Young, Y.L., 2021. 3-D high-fidelity hydrostructural optimization of cavitation-free composite lifting surfaces. Compos. Struct. 268, 113937. http://dx.doi.org/10.1016/j.compstruct.2021.113937.

Linton, C.M., Evans, D.V., 1993. The interaction of waves with a row of circular cylinders. J. Fluid Mech. 251, 687–708. http://dx.doi.org/10.1017/S002211209300357X.

Liu, Y., 2019. HAMS: A frequency-domain preprocessor for wave-structure interactions-Theory, development, and application. J. Mar. Sci. Eng. 7 (3), 1–19. http://dx.doi.org/10.3390/jmse7030081.

MacCamy, R.C., Fuchs, R.A., 1954. Wave forces on piles: A diffraction theory.

Martins, J.R.R.A., Ning, A., 2021. Engineering Design Optimization. Cambridge University Press, http://dx.doi.org/10.1017/9781108980647.

McCabe, R., Murphy, O., Haji, M., 2022. Multidisciplinary optimization to reduce cost and power variation of a wave energy converter. Proc. ASME Des. Eng. Tech. Conf. 3-A, 1–10. http://dx.doi.org/10.1115/DETC2022-90227.

Morison, J., O'Brien, M., Johnson, J., Schaaf, S., 1950. The force exerted by surface waves on piles. J. Pet. Technol. 2 (05), 149–154. http://dx.doi.org/10.2118/950149-G.

Newman, J.N., 2017. Marine Hydrodynamics, fortieth ed. The MIT Press, Cambridge, Massachusetts, p. 450. http://dx.doi.org/10.7551/mitpress/4443.001.0001.

Ng, G.W., Martins, J.R., Young, Y.L., 2022. Optimizing steady and dynamic hydroelastic performance of composite foils with low-order models. Compos. Struct. 301, 116101. http://dx.doi.org/10.1016/j.compstruct.2022.116101.

Pegalajar-Jurado, A., Borg, M., Bredmose, H., 2018. An efficient frequency-domain model for quick load analysis of floating offshore wind turbines. Wind Energy Sci. 3 (2), 693–712. http://dx.doi.org/10.5194/wes-3-693-2018.

Pollini, N., Pegalajar-Jurado, A., Bredmose, H., 2023. Design optimization of a TetraSpar-type floater and tower for the IEA Wind 15 MW reference wind turbine. Mar. Struct. 90, 103437. http://dx.doi.org/10.1016/j.marstruc.2023.103437.

Rohrer, P.J., Bachynski-Polić, E.E., Collette, M., 2022. Towards gradient-based design optimization of fully-flexible tension-leg platform wind turbines. J. Phys. Conf. Ser. 2362 (1), http://dx.doi.org/10.1088/1742-6596/2362/1/012033.

Rohrer, P.J., Bachynski-Polić, E.E., Hegseth, J.M., 2023. Gradient-based design optimization of fully-flexible floating wind turbines using modal analysis. In: Ocean Renewable Energy, vol. 8, American Society of Mechanical Engineers, pp. 1–10. http://dx.doi.org/10.1115/OMAE2023-101930.

Sharp, C., DuPont, B., 2016. A multi-objective real-coded genetic algorithm method for wave energy converter array optimization. In: Ocean Space Utilization; Ocean Renewable Energy, vol. 6, American Society of Mechanical Engineers, pp. 1–10. http://dx.doi.org/10.1115/OMAE2016-54996.

Sykes, V., Collu, M., Coraddu, A., 2023. A review and analysis of optimisation techniques applied to floating offshore wind platforms. Ocean Eng. 285 (P1), 115247. http://dx.doi.org/10.1016/j.oceaneng.2023.115247.

Yeung, R.W., 1981. Added mass and damping of a vertical cylinder in finite-depth waters. Appl. Ocean Res. 3 (3), 119–133. http://dx.doi.org/10.1016/0141-1187(81)90101-2.

Zhang, J., Taflanidis, A.A., Scruggs, J.T., 2020. Surrogate modeling of hydrodynamic forces between multiple floating bodies through a hierarchical interaction decomposition. J. Comput. Phys. 408, 109298. http://dx.doi.org/10.1016/j.jcp.2020.109298.